Plasmonic modes of polygonal rods calculated using a quantum hydrodynamics method

Kun Ding and C. T. Chan[*]

Department of Physics and Institute for Advanced Study, The Hong Kong University of Science and Technology, Clear Water Bay, Hong Kong

Plasmonic resonances of nanoparticles have drawn lots of attention due to their interesting and useful properties such as strong field enhancements. The self-consistent hydrodynamics model has the advantage that it can incorporate the quantum effect of the electron gas into classical electrodynamics in a consistent way. We use the method to study the plasmonic response of polygonal rods under the influence of an external electromagnetic wave, and we pay particular attention to the size and shape of the particle and the effect of charging. We find that the particles support edge modes, face modes, and hybrid modes. The charges induced by the external field in the edge (face) modes mainly localize at the edges (faces), while the induced charges in the hybrid modes are distributed nearly evenly in both the edges and faces. The edge modes are less sensitive to particle size than the face modes but are sensitive to the corner angles of the edges. When the number of sides of regular polygons increases, the edge and face modes gradually change into the classical dipole plasmonic mode of a cylinder. The hybrid modes are found to be the precursor of the Bennett mode, which cannot be found in classical electrodynamics.

I. INTRODUCTION

Plasmonic resonances are ubiquitous for metallic nanoparticles [1–8], and these collective excitation modes can be used to realize many interesting phenomena, such as extraordinary optical transmission [7] and negative refraction [8]. Recent advances in nanoscience enabled the fabrication of metallic nanoparticles with controlled size and shape. At the nanoscale, the quantum nature of electrons emerges [9–26] and standard local electrodynamics description becomes inadequate. For example, nonlocal effects must be taken into consideration in order to study the resonances of nanometallic particles, as have already been verified experimentally [9,10]. In addition to the nonlocal effect, other quantum effects are also not ignorable in plasmonic modes [11–26]. One issue is the tunneling of the electrons through tiny gaps for gap plasmonic modes in the core shell structure [11–13] and dimer structures [14–17], which reduces the field enhancement. Another quantum feature is the loss caused by the surrounding material due to the creation of surface electron-hole pairs [25,26]. In order to describe these quantum effects theoretically, different methods have been proposed [27–50]. The most accurate formulation that is computationally tractable is perhaps the time-dependent density functional theory (TD-DFT) [27–33]. This method is already computationally intensive, and the computation becomes even more demanding if TD-DFT is coupled with Maxwell equations to include electromagnetic (EM) wave characteristics, such as retardation [51,52]. On the other hand, corrected classical models, such as nonlocal surface layer models [34–36], hard-wall hydrodynamics models [37–40,53], quantum corrected models [41–43], and others [44,45], have also been proposed to study these systems. These models can handle full EM wave characteristics, in the sense that Maxwell equations are explicitly and exactly solved, but some quantum features of the electron gas are not included. For example, the electron spill-out effect near the metal surface [46] is typically not treated adequately. The self-consistent

hydrodynamics model (SC-HDM) [46–50] can be viewed as an advanced form of quantum corrected classical model. This model works with the electron density instead of electronic wave functions, so that the energy functional is simple enough to solve for the response equations and Maxwell equations at the same time and on the same footing self-consistently [46–50]. This method has been employed successfully to study the plasmonic responses for some simple plasmonic structures with simple geometries [46–50]. The power of this method is its ability to handle systems with complex structure and complex geometry, and it is worthwhile to study the EM wave response of some complicated metallic particles using this model.

In this paper, we employ the SC-HDM to investigate the plasmonic modes of polygonal rods. We found three types of plasmonic modes, namely edge, face, and hybrid modes. In the edge (face) modes, the charges induced by an external EM wave are mainly localized at the edges (faces), while in the hybrid modes, the induced electrons are distributed nearly evenly in both edges and faces. The resonance frequency of the edge modes are mainly determined by the corner angles of the edges, while the face modes are more sensitive to particle sizes. In addition, when the number of sides of regular polygons increases, the edge and face modes merge into the classical dipole plasmonic mode of a cylinder. The hybrid modes are found to be the precursor of the Bennett mode, which originates from charge oscillating in and out of a surface. The paper is organized as follows. In Sec. II, we briefly review the SC-HDM. The numerical results of ground states for charge neutral particles are given in Sec. III. In Sec. IV, we calculate the scattering properties of these polygonal rods, such as absorption spectrum, plasmonic mode profile, geometric effect, energy dissipation distributions, and the effect of charging. Conclusions are drawn in Sec. VI.

II. FORMULATION OF SC-HDM

The systems studied are two-dimensional (2D) polygonal rods, as shown in Fig. 1(a). The polygonal rods are translational invariant along the z axis. The yellow regions stand for the

---
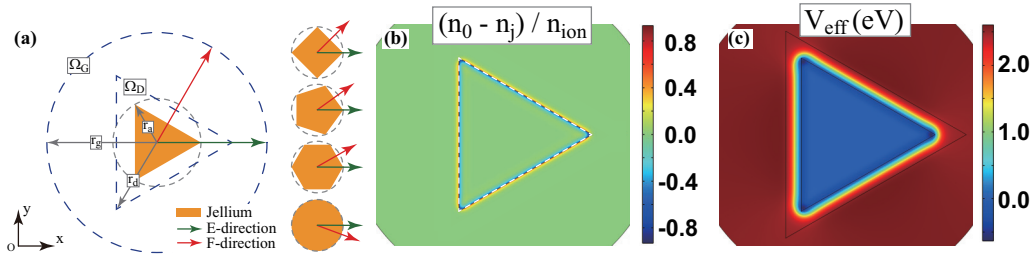
[*]Corresponding author: phchan@ust.hk

FIG. 1. (a) Schematic picture of the plasmonic system under consideration, in which yellow region stands for the jellium background with circumradius r_a, Ω_G is the ground state calculation domain with radius r_g, and Ω_D is the excited state calculation domain with radius r_d. The right inset shows different regular polygons with the same circumradius r_a. The green (red) arrow denotes the edge (face) direction of the regular polygons. Calculated electron distribution $(n_0 - n_j)/n_{ion}$ and effective potential V_{eff} of the ground state for a sodium triangle with radius $r_a = 2$ nm is shown in (b) and (c), respectively. The white dashed line in (b) highlights the jellium boundaries. The VW parameter λ_ω (see text) is chosen as 0.12, the radius of excited state calculation domain is $r_d = 2.7$ nm, and that for ground state calculation domain is $r_g = 3.5$ nm.

jellium background in the shape of regular polygons. They are bounded by a circumscribed circle with radius r_a, as marked by the gray dashed lines in Fig. 1(a). The right inset in Fig. 1(a) shows polygonal rods with different side numbers N. The blue dashed circle and triangle show the boundaries of ground state and scattering state calculation domain, respectively, denoted by Ω_G and Ω_D.

To study the plasmonic response of our system, we employ a SC-HDM [46–50]. The SC-HDM is well documented in the literature [46–50], but to make the descriptions self-contained, we will give a short introduction of the model in this section. The basic assumption of a hydrodynamics model (HDM) is to treat the electrons of metals as ideal, irrotational, and isentropic fluid, which indicates that temperature effects are not included in the model. Based on these assumptions, the electron gas can be described by the physical variables, electron density $n(\mathbf{r},t)$, and canonical momentum $\mathbf{p}(\mathbf{r},t)$. The equations of motion for the electron gas can be obtained from the time evolutions of these variables, namely [46–50]

$$m_e n\left(\frac{\partial \mathbf{v}}{\partial t} + \mathbf{v} \cdot \nabla \mathbf{v}\right) = -n\nabla\left(\frac{\delta G}{\delta n}\right) + nq_e(\mathbf{E} + \mathbf{v} \times \mathbf{B}),$$
(2.1)

$$\frac{\partial n}{\partial t} + \nabla \cdot (n\mathbf{v}) = 0,$$
(2.2)

where $q_e = -e$ is the charge of the electron ($e > 0$), m_e is the mass of the electron, $\mathbf{v} = (\mathbf{p} - q_e\mathbf{A})/m_e$ is the velocity of the electron, $\mathbf{A}$ is the vector potential, and $\mathbf{E},\mathbf{B}$ are the fields generated by the charges, currents, and external EM waves. The functional $G[n(\mathbf{r},t)]$ is the internal energy of the electron gas, including the internal kinetic energy and the exchange-correlation energy [54–56]. In this paper, we follow the choice of $G[n(\mathbf{r},t)]$ in Ref. [47] (see also Supplemental Material, Sec. I [57]). Equations (2.1) and (2.2) are the basic equations in the HDM, and their numerical solutions together with the Maxwell equations are needed to study the plasmonic behavior of our system.

The next step is to do linear expansions of the following quantities in Eqs. (2.1) and (2.2) as

$$n = n_0 + n_1, \quad \mathbf{v} = \mathbf{v}_1, \quad \left(\frac{\delta G}{\delta n}\right) = \left(\frac{\delta G}{\delta n}\right)_0 + \left(\frac{\delta G}{\delta n}\right)_1,$$

$$\mathbf{E} = \mathbf{E}_0 + \mathbf{E}_1, \quad \mathbf{B} = \mathbf{B}_1,$$
(2.3)

where the subscript 0 stands for the equilibrium states and subscript 1 means the linear expansions of these quantities. The equilibrium $\mathbf{v}_0$ is zero, which means no electrons move at equilibrium, and $\mathbf{B}_0$ is also zero because no external static magnetic field is imposed. Substitute the expansions in Eq. (2.3) into Eqs. (2.1) and (2.2) and Maxwell equations, and keep the zero order terms. Then we arrive at

$$\left(\frac{\delta G}{\delta n}\right)_0 + q_e\phi_0 = \mu,$$
(2.4)

$$\nabla^2\phi_0 = \frac{q_e}{\varepsilon_0}(n_+ - n_0),$$
(2.5)

where μ is the chemical potential, n_0 is the ground state electron density, and ϕ_0 is the electrostatic potential defined as $\mathbf{E}_0 = -\nabla\phi_0$. Here, n_+ stands for the positive charged background including nuclei and core electrons. Here, we use the jellium model $n_+ = n_j$, in which $n_j = n_{ion}$ inside the metal, and $n_j = 0$ outside the metal. The ion density n_{ion} is defined via a dimensionless quantity r_s as

$$n_{ion} = \frac{3}{4\pi(r_s a_H)^3},$$
(2.6)

where $a_H = 0.529\,\text{Å}$ is the Bohr radius. The total number of electrons imposes another constraint [46,58]. Suppose the particle has a net charge σ. Then the electron density should obey

$$\int_{\Omega_G} d\mathbf{r}\, e[n_+ - n_0] = \sigma.$$
(2.7)

Equations (2.4), (2.5), and (2.7) collectively determine the ground state charge densities of the plasmonic particles.

The linear response equations in the frequency domain could be obtained by keeping the first order terms in the expansions of Eqs. (2.1) and (2.2) and Maxwell equations, namely [46–50]

$$(-i\omega + \gamma)\mathbf{J}_1 = \frac{en_0}{m_e}\nabla\left(\frac{\delta G}{\delta n}\right)_1 + \frac{e^2 n_0}{m_e}\mathbf{E}_1,$$
(2.8)

$$\nabla \cdot \mathbf{J}_1 - i\omega\rho_1 = 0,$$
(2.9)

$$\nabla \times (\nabla \times \mathbf{E}_1) - \left(\frac{\omega}{c}\right)^2 \mathbf{E}_1 = i\omega\mu_0\mathbf{J}_1,$$
(2.10)

where the induced currents and charges are defined as $\mathbf{J}_1 = n_0 q_e \mathbf{v}_1$ and $\rho_1 = q_e n_1$, γ is the loss parameter introduced empirically here [59,60], and the electric fields $\mathbf{E}_1 = \mathbf{E}_{\text{inc}} + \mathbf{E}_{\text{sca}}$ are total fields including incident fields and scattering fields from the environment. Equations (2.8)–(2.10) determine the linear responses of the plasmonic particles.

Before going into the details, we note that the loss introduced within this method is empirical because the method does not include any microscopic loss mechanism, such as electron-phonon scattering and the production of bulk or surface electron-hole pairs. It is known that these loss mechanisms are quite sensitive to the surrounding media because of the screening effect. In order to compare our results quantitatively with experimental ones, the empirical loss parameter needs to be set depending on the real surroundings. Furthermore, the loss parameter should also rely on the mode profile of the plasmonic resonance because of electron-hole pair productions [25]. Since the plasmonic resonance is a kind of charge density oscillation, the production of electron-hole pairs created at different plasmonic resonances should depend on the charge distributions of the mode. In other words, the loss parameter should in principle depend on the mode characteristics.

Two numerical steps are needed to obtain the plasmonic resonances and related properties of the system using SC-HDM. We first solve Eqs. (2.4), (2.5), and (2.7) to get the ground states, and then solve Eqs. (2.8) to (2.10) to get the scattering states. In the following sections, we will discuss the numerical implementations of the models and some numerical results of polygonal rods.

III. GROUND STATE OF CHARGE DENSITY OF NEUTRAL POLYGONAL RODS

In this section, we consider the ground state density for the charge neutral polygonal rods. We employ a finite element method (FEM) to solve the differential Eqs. (2.4), (2.5), and (2.7) in real space [61,62], and numerical details are given in the Supplemental Material, Sec. II [57]. For simplicity's sake, we will assume throughout this paper that the jellium represents the simple metal sodium. In the numerical calculations, the ground state calculation domain is denoted by Ω_G, the boundary of which is shown by blue dashed lines in Fig. 1(a). In the energy functional, the parameter λ_ω comes from von Weizsacker kinetic energy functional [54,55]. Throughout this paper, we set λ_ω to 0.12, as this is optimal for our calculations (see Supplemental Material, Sec. IV [57]).

The calculated electron density n_0 distributions of the ground state for a sodium ($r_s = 4$) triangle with radius $r_a = 2$ nm is shown in Fig. 1(b). To show the difference between the electron density and jellium background, we plot the relative dimensionless quantity $(n_0 - n_j)/n_{\text{ion}}$ in Fig. 1(b) to demonstrate the ground state charge densities. The white dashed line shows the boundaries of the jellium background. We note that the electron density distributions are smooth near the edges of the jellium background, although the jellium background density does have singularities at the polygon corners. As expected, the electron density is equal to the jellium background in the bulk metal region. The difference between the electron density and jellium background only occurs near the surfaces, creating a surface dipole layer. The existence

of this dipole layer forms an electrostatic potential barrier, which constitutes one part of the effective single electron potential $V_{\text{eff}}(\mathbf{r})$ (see Supplemental Material, Sec. II, for the explicit formulations of $V_{\text{eff}}(\mathbf{r})$ [57]). To see this, we plot the corresponding effective single electron potential $V_{\text{eff}}(\mathbf{r})$ in Fig. 1(c). The zeros of the effective potential are set to the chemical potential deep inside the metal. The distribution of $V_{\text{eff}}(\mathbf{r})$ is anisotropic, indicating that the surface dipole layer in the edge direction (E direction), denoted by the green arrow in Fig. 1(a), are quite different from that in the face direction (F direction), labeled by the red arrow in Fig. 1(a). It should be mentioned that our calculations are in 2D space, with the z direction being invariant, so the corner in 2D space is the edge in the three-dimensional (3D) space, and the edge in 2D space is the face in 3D space. Throughout this paper, we will use the notations in 3D space.

To further see the effect of the sharp edges on the surface dipole, we plot the modulation of the local work function as a function of polar angles θ/π for a sodium triangle by gray lines in Fig. 2(a). The local work function $W_F(\theta)$ is defined as $W_F(\theta) = V_{\text{eff}}(\theta, r = r_g) - V_{\text{eff}}(\theta, r = 0)$, which r and θ are radial and angular coordinates in the polar coordinate system. Since the cylinder is isotropic, we choose the work function of a sodium cylinder as the reference, marked by magenta lines in Fig. 2(a). The gray line in Fig. 2(a) shows that the local work function in the E direction is lower than that in the F direction. For comparison, we also plot the local work function distributions for a sodium square, pentagon, hexagon, and 20-sided polygon in Fig. 2(a) by orange, red, blue, and green lines, respectively. As the number of sides of the regular polygon increases, the local work function difference between polygons and cylinder becomes smaller because the corners of the polygon are smoother. The local work function difference between E and F directions is also smaller with the increasing of side number. To show this, we plot the relative local work functions versus the half of the interior angle ($\alpha = \frac{\pi}{2}(1 - \frac{2}{N})$) of a regular polygon in Fig. 2(b) for the E and F directions by open squares and open triangles, respectively. It can be seen that, as α increases, the difference between the edge and face direction gets smaller. As far as the ground state is concerned, the key difference between polygons and the circle is the anisotropic local work function, indicating different surface dipoles in different angles. This is a geometric curvature effect, in contrast to the crystal plane (packing) induced work function difference [63].

IV. SCATTERING PROPERTIES OF POLYGONAL RODS

After obtaining the ground state density, we can implement the linear response equations into FEM. The numerical details are given in the Supplemental Material, Sec. III [57]. To get the scattering state accurately, the total calculation domain (Ω_T) must be of the wavelength order. As we are concerned with the deep subwavelength properties of the plasmonic resonances, the particle size is much smaller than the wavelength. In order to deal with the scale difference between the particle size and the wavelength, we divide the total calculation domain into two subdomains. One is the domain near the particle denoted by Ω_D within which we solve the full linear response equations, and the other subdomain $\Omega_F (\equiv \Omega_T - \Omega_D)$ is the
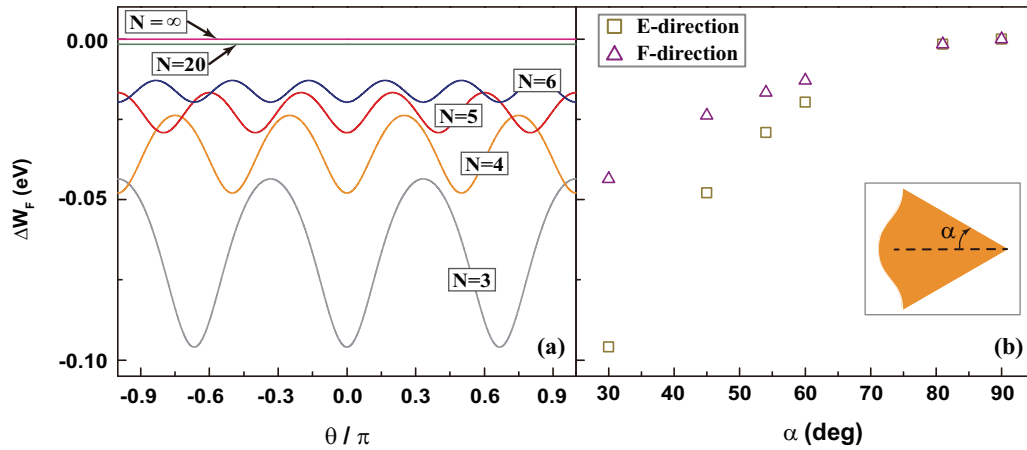
FIG. 2. (a) Modulations of local work function as a function of polar angle θ/π for a triangle, square, pentagon, hexagon, 20-sided polygon, and cylinder are plotted by gray, orange, red, blue, green, and magenta lines, respectively. (b) Local work functions in the E (edge) direction and F (face) direction as a function of interior angles α are plotted by open squares and open triangles, respectively. The circumradii of all the regular polygons are 2.0 nm.

free space within which we only solve Maxwell equations. The subdomain Ω_D, with a finer grid than Ω_F, is chosen to make sure that there are no induced electrons outside this domain, so we do not need to solve linear response equations outside. Throughout this paper, we set the radius r_d of Ω_D to $r_d = r_a + 0.7$ nm, and this setting is optimal for our calculations (see Supplemental Material, Sec. V [57]).

A. Absorption spectrum and mode profile

To see the plasmonic modes of polygonal rods, we calculate the absorption cross-section σ_{abs} under plane wave illumination with incident angle $\theta_i = 0$ ($\mathbf{E} \| \mathbf{y}$) for the triangle and square, as shown in Figs. 3(a) and 3(b) by solid blue/red lines, respectively. The incident angle θ_i is defined as the polar angle of the wave vector, and the coordinates are given in Fig. 1(a). The values of σ_{abs} are calculated by integrating the Poynting vector in the far field. From Figs. 3(a) and 3(b), several prominent absorption peaks are found in the spectra for both the triangle and square. The frequency of resonance peaks shows strong dependence on the geometry. If we characterize the resonances according to the pattern of induced charge concentration, we can group them into three categories: edge modes (Ed mode), face modes (Fa mode), and hybrid modes (Hb mode). The edge (face) modes have the induced electrons mainly localize at the edges (faces). In the hybrid modes, the induced electrons are distributed nearly evenly in both edges and faces and also have a notable local in-and-out oscillation perpendicular to the interfaces. Using this classification, we labeled the plasmonic modes by Ed, Fa, and Hb in Fig. 3. For instance, the symbol Ed_1^T is used to denote the first (subscript 1 is the mode index) edge (Ed) mode for triangle (superscript T) particles. The lowest frequency modes for both the triangle and square are found to be edge modes. The induced charge and current distributions of the Ed_1^T mode and Ed_1^S mode are plotted in Figs. 4(a) and 4(c), respectively. The color stands for the quantity ρ_1/E_0 and the arrows represent $\mathbf{J}_1$ at some particular time. It is clear that the induced electrons are mainly concentrated near the edges. There are also high order edge modes, such as Ed_2^T. The induced electrons in these modes

still mainly localize near the edges, but they decay into the face slower than the fundamental mode.

The face modes for triangle and square appear in higher frequencies, as shown by Fa_1^T and Fa_1^S in Figs. 3(a) and 3(b). The induced charge and current distributions of Fa_1^T and Fa_1^S modes are shown in Figs. 5(a) and 5(c), respectively. Compared with the Ed modes, Fa modes have their induced electrons mainly localized near the polygon faces, with the currents flowing from one face to another. The induced charges have opposite signs for a single face, but the amplitudes of the positive and negative charges are different. In Figs. 3(a) and 3(b), the further higher frequency modes are hybrid modes, denoted by Hb^T and Hb^S. The bandwidths of them are broad due to more dissipative loss, and the induced charges are in both edges and faces.

For comparison, solid gray lines in Figs. 3(a) and 3(b) show the absorption spectrum of the triangle and square calculated by the classical model. The classical model is equivalent to the SC-HDM under local response approximations (LRAs, see also Supplemental Material, Sec. VI [57]), which ignores the $\frac{\delta G}{\delta n}$ term and sets $n_0 = n_j$. In order to make a meaningful comparison with SC-HDM results, we need to smooth the sharp edges of the polygonal rods within LRA calculations. It is because the electron distributions in SC-HDM are always smooth over the sharp edges of the jellium background (due to the kinetic term in the energy functional), as shown in Fig. 1(b) [31,64], but there is no smoothing mechanism in classical LRA calculations. According to the electron densities calculation by SC-HDM, we set the smoothing length to 0.1 nm in Fig. 3 (see Supplemental Material, Sec. VII [57]). We also see several prominent absorption peaks in the spectrum. The modes could be classified into two classes. The lower frequency peaks (below 4 eV) are edge modes, while the higher frequency peaks can be assigned as the face modes. This classification is possible because there are two branches of plasmonic modes for a single metallic wedge according to prior quasistatic solutions of the wedge problem [65,66]. The lower frequency band has even symmetry, while the higher frequency band consists of odd modes. For the even mode, the induced charges on the two faces of the wedge are the same, so the induced
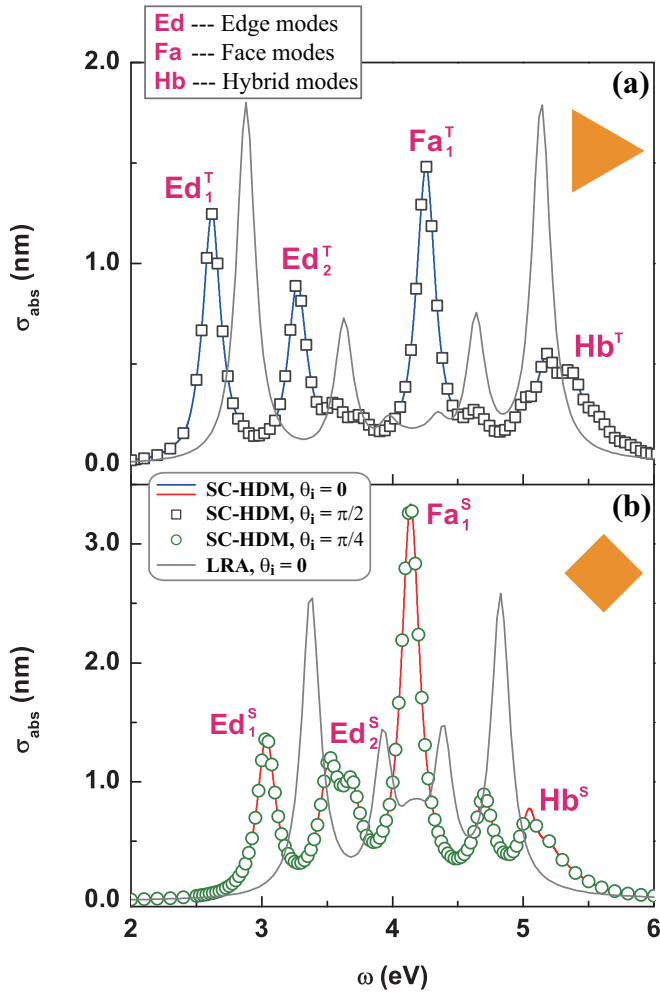
FIG. 3. Absorption spectra of (a) a triangle and (b) a square with circumradius $r_a = 2$ nm under plane wave incidence with incident angle $\theta_i = 0$ are plotted by blue and red solid lines, respectively. The loss parameter γ is 0.17 eV throughout the domain Ω_D. The absorption spectrum of triangle for plane wave with incident angle $\theta_i = \pi/2$ is plotted in (a) by gray dots, and that of square for plane wave with incident angle $\theta_i = \pi/4$ is plotted in (b) by green dots. The gray lines show the absorption spectra calculated by the classical model with the rounded corners (see text). The resonance modes are labeled according to their induced charge profiles (see text). The superscript denotes the shapes (T stands for triangle) and the subscript denotes the mode number.

charges are maximal in the corner position. Symmetry-wise, this corresponds to the edge modes observed in SC-HDM. For the odd modes, the induced charges of the two faces have opposite signs, so there must be a node in the corner position. This corresponds to the face modes observed in SC-HDM. These classical results help us understand the modes in SC-HDM qualitatively, but they are significantly shifting in frequency due to quantum spill out effects [67]. We will discuss the physical reasons for the quantum corrections later.

We now change the incident angle θ_i of the plane wave, but keep the incident electric fields in the xy plane, and then calculate absorption spectrum again. For triangle particles, we plot the absorption spectrum for a plane wave with incident

angle $\theta_i = \pi/2$ in Fig. 3(a) by open gray dots. We see that the absorption spectrum is almost the same as the spectrum for the $\theta_i = 0$ case. This is because the particle size is much smaller than the wavelength, and as such, the EM wave cannot recognize the anisotropy of the metallic particles [68], and hence, the external wave couples equally well with the particle resonances irrespective of the incident angle. We plot the induced charges and currents under this plane wave incidence of Ed_1^T and Fa_1^T modes in Figs. 4(b) and 5(b), respectively. The induced electrons are still localized in edges and faces for these modes even though the polarizations of the incident waves are different. These results further show that the peaks correspond to intrinsic resonant modes. For the square particle, the absorption spectrum under plane wave illumination ($\theta_i = \pi/4$) is also plotted by green dots in Fig. 3(b). The induced charges and currents of Ed_1^S and Fa_1^S modes are plotted in Figs. 4(d) and 5(d), respectively. We note that these edge and face modes also exist for various geometric configurations, and they are experimentally observed in different plasmonic particles [1,69,70].

Before going to the next section, we note that the computational time of our method is much less than *ab initio* packages, such as TD-DFT that incorporates Maxwell equations. The cost of computational time of our method is about one order of magnitude longer than classical models (see Supplemental Material, Sec. VIII [57]).

B. Geometric effect

In the previous section, we see that polygonal metallic particles carry resonances that can be classified as edge modes, face modes, and hybrid modes. For a cylindrical rod, there are two plasmonic resonances: the classical dipole resonance (D mode), and the Bennett mode (M mode, also known as multipole surface plasmon modes) [71–73]. It is interesting to see how the resonance modes in polygonal rods approach those of the cylinder as the number of corners increases. We will consider the effect of side number of the regular polygon while keeping either the radius r_a fixed or the total number of electrons fixed. To see this geometric effect, we show the calculated absorption spectra for various N-sided polygons and cylindrical particles with the same radius in Fig. 6(a). The absorption spectra for these polygonal rods with the same total number of electrons are plotted in Fig. 6(b). We see that the edge and face modes come together and become the dipole mode as the side number N increases. We note that the dipole resonance frequency of the cylindrical rod is 3.96 eV according to our calculations. This is consistent with Refs. [48,67], which is redshifted comparing with classical resonance frequency $\omega_p/\sqrt{2} = 4.16$ eV (see Supplemental Material, Sec. VI [57]). Although our choice of the exchange-correlation terms in energy functional $G[n(\mathbf{r},t)]$ is different from Refs. [48,49], the dipole resonance peak is essentially the same, indicating that the plasmon resonances are not sensitive to the details of the exchange-correlation potential in the energy functional.

The Bennett mode of cylindrical rods corresponds to a perpendicular oscillation of the electron density in and out of the surface of the plasmonic particle along the radial direction. The induced charges have opposite signs but the
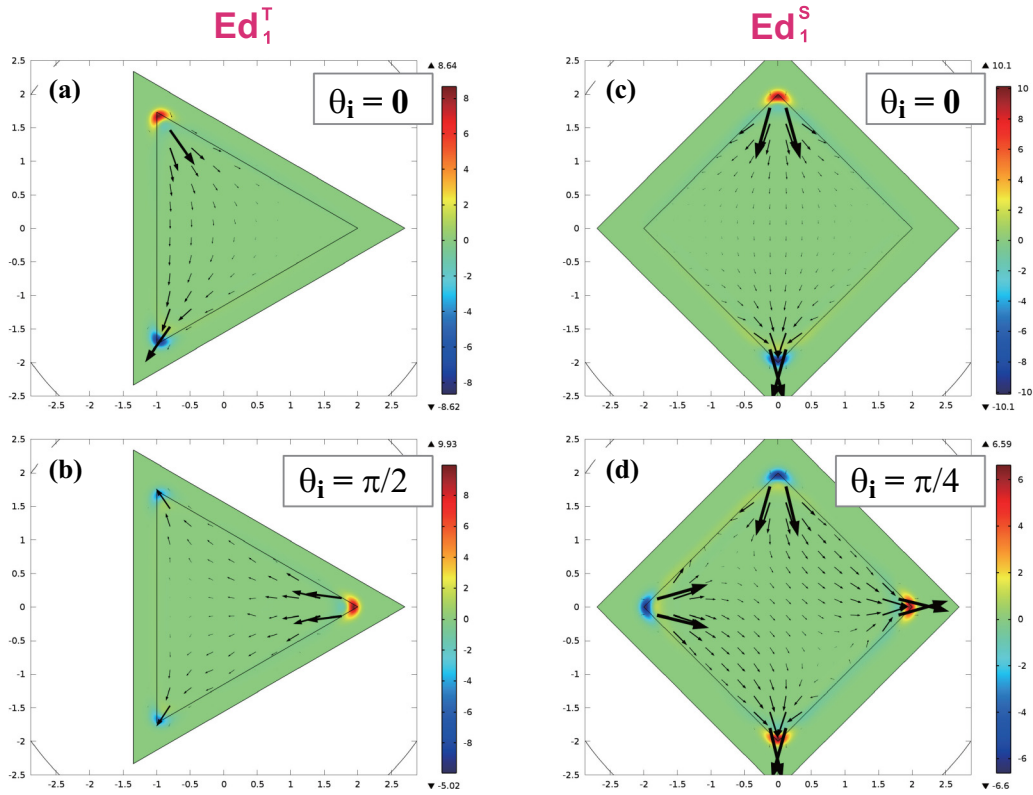
FIG. 4. Plot of the induced electron density ρ_1/E_0 (color/intensity) and the current density $\mathbf{J}_1$ (vector field) at some particular time for the Ed_1^T mode shown in Fig. 3 for a plane wave incident at an angle (a) 0 and (b) $\pi/2$, respectively. The induced electron density and current density for the Ed_1^S mode are shown in (c) and (d) for plane wave incident angle 0 and $\pi/4$, respectively.
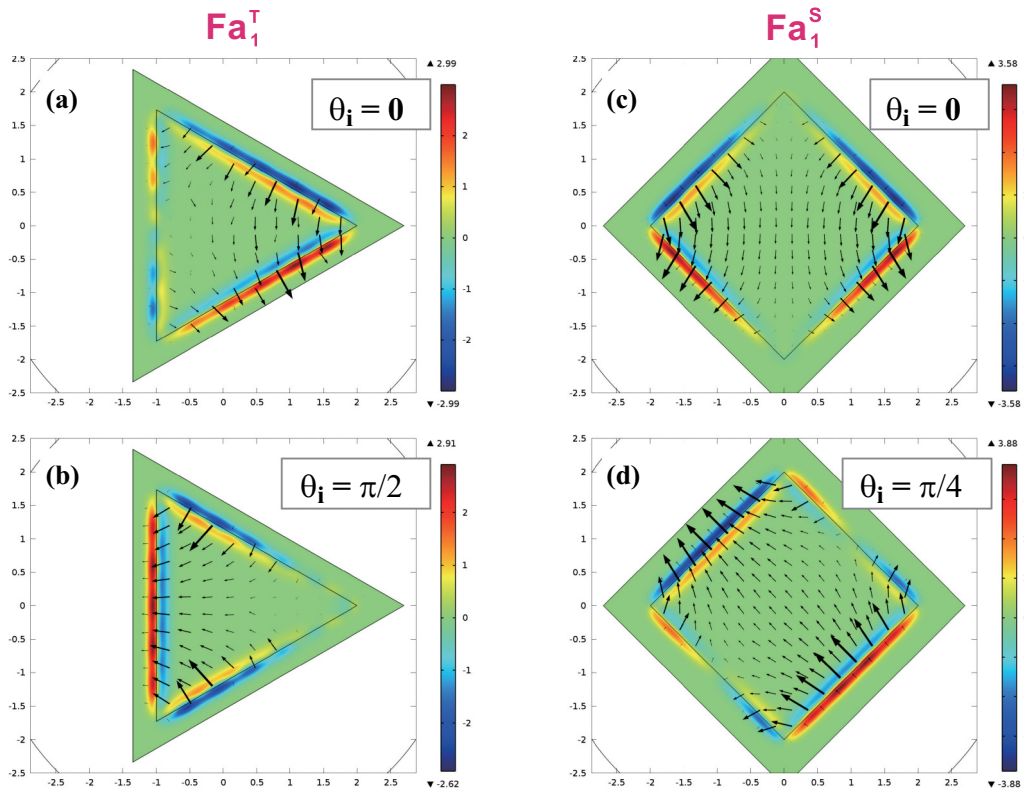

FIG. 5. Plot of the induced electron density ρ_1/E_0 (color/intensity) and the current density $\mathbf{J}_1$ (vector field) at some particular time for the Fa_1^T mode claimed in Fig. 3 are shown in (a) and (b) for plane wave incident at angles of 0 and $\pi/2$, respectively. The induced electron density and current density for the Fa_1^S mode are shown in (c) and (d) for plane wave incident at angles 0 and $\pi/4$, respectively.
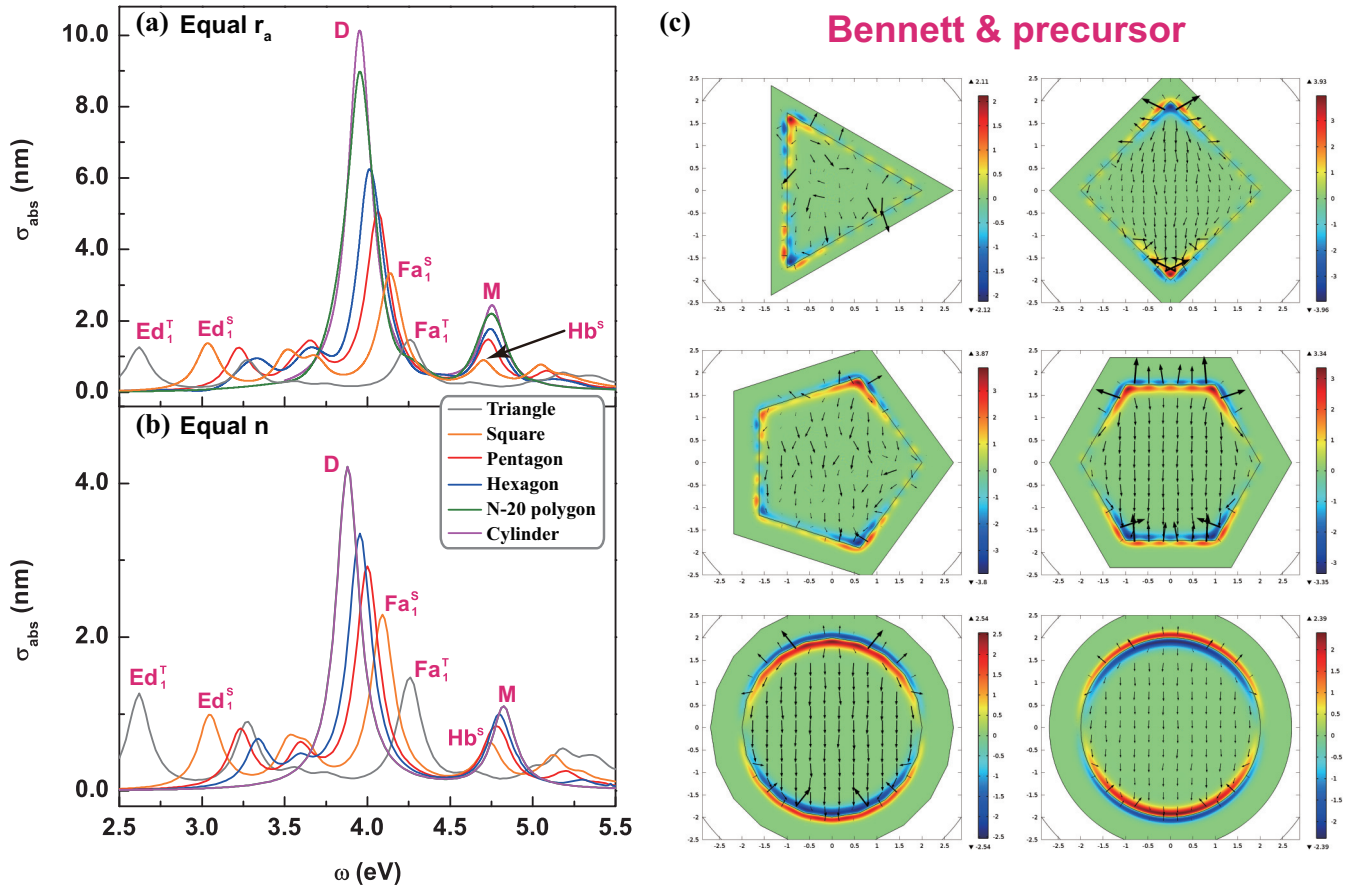
FIG. 6. (a) Absorption spectra of regular polygons with increasing side number N are plotted by the solid lines. All regular polygons have the same circumradius $r_a = 2.0$ nm, and loss parameter γ is 0.17 eV throughout the domain Ω_D. (b) Absorption spectra of polygons with increasing side number N for fixed total number of electrons. (c) Induced electron density ρ_1/E_0 (color/intensity) and current density $\mathbf{J}_1$ (vector field) at some particular time for the Bennett mode and its precursors [the M and Hb modes shown in (a)].

same amplitude normal to the surface of one single face so that a single face is locally charge neutral for the Bennett mode, while that for the dipole mode is nonneutral [71–73]. The Bennett mode can only exist in models which allow the electron spill out effect (see Supplemental Material, Sec. VI [57]) so that charge can oscillate from inside the metal into the vacuum. According to our model, the resonance frequency of the Bennett mode is 4.76 eV, as shown by magenta lines in Fig. 6(a). From Figs. 6(a) and 6(b), we see that the hybrid modes of regular polygons can be treated as the precursors of the Bennett mode in the circular cylinder. The hybrid mode is very weak for the triangular particle, as shown by gray lines in Fig. 6(a). The hybrid mode absorption peak increases as the side number of the polygon increases, as shown by orange, red, blue, and green lines in Fig. 6(a), eventually merging with the Bennett mode peak. In order to see how the hybrid modes change into the Bennett mode, we plot in Fig. 6(c) the induced electron densities and currents of the hybrid mode peaks in Fig. 6(a) for different polygonal rods. We see that, in addition to a local oscillation component, the Bennett mode also has global components due to the finite size of the particle. When the side number decreases, the local components gradually decrease while the global components increase and finally become the hybrid mode.

The results so far indicate that the edges in polygonal rods can strongly modify the plasmonic resonances of small particles, splitting the dipole resonance into edge/face modes that can be significantly redshifted/blueshifted, depending on the angle of the wedge. Comparison of our SC-HDM results with classical model results (e.g. Fig. 3) also indicate that nonlocal effects are significant and cannot be ignored.

In addition to shape, size is obviously another parameter that can control plasmonic resonances. The size dependence of plasmonic modes directly relates to the dispersion relations of these plasmonic modes [74–76]. We plot the resonance frequencies of the Ed_1^T mode and Ed_1^S mode as a function of particle size r_a^{-1} in Fig. 7(a) by solid red and blue lines. We see that the edge mode frequencies of both the triangle and square are nearly independent of the particle size in this range. This is consistent with the fact that the induced charges are mainly bounded to the single edge, so the size effect is minimal here. For comparison, we also calculate the size dependence of the Ed_1^T mode and Ed_1^S mode using the classical model, as shown by the dashed red and blue lines in Fig. 7(a). Similar to the SC-HDM, classical models also show little size dependence of these edge modes. However, the edge mode frequencies within SC-HDM are redshifted comparing to LRA, which are similar to the dipole mode of a cylindrical rod. The physical reason
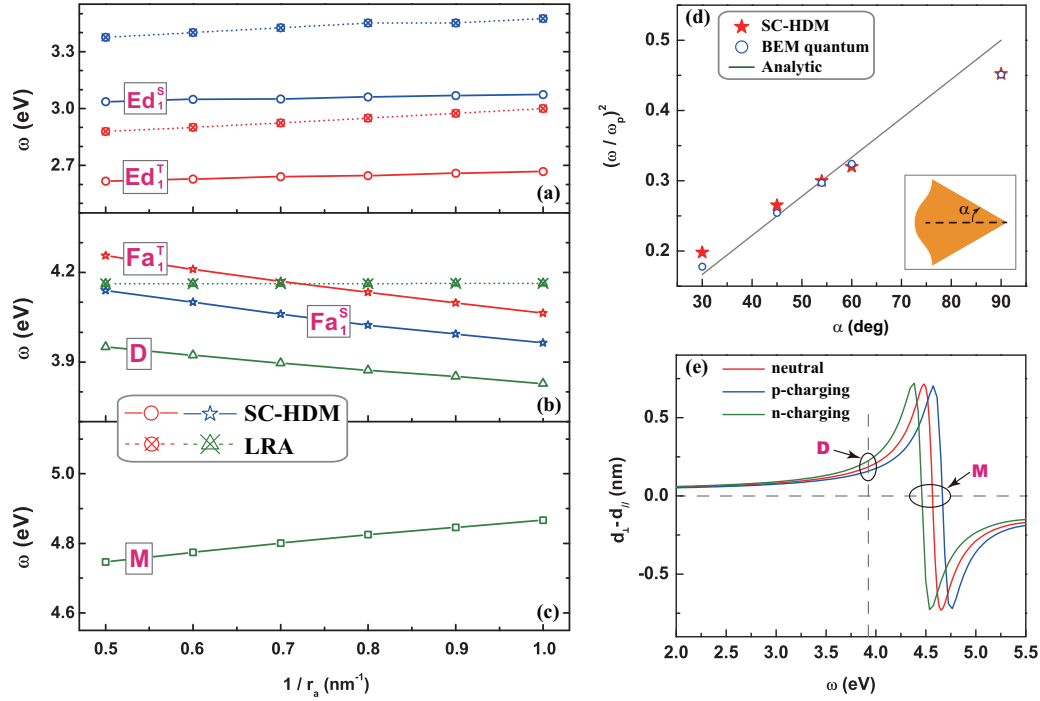
FIG. 7. (a) The resonance frequencies of the edge modes as a function of the circumradius is plotted by red circles (Ed_1^T mode) and blue circles (Ed_1^S mode), respectively. The open circles are obtained by SC-HDM, and the circles with a cross inside are obtained using classical model (LRA). (b) The resonance frequencies of the face modes as a function of the radius are plotted by red stars (Fa_1^T mode) and blue stars (Fa_1^S mode), respectively. The resonance frequencies of the dipole mode (D mode) for cylindrical particles are also plotted by dark green triangles. (c) The resonance frequencies of the Bennett mode (M mode) for cylindrical particles are plotted by dark green squares. (d) The calculated resonance frequencies of the Ed_1 mode for SC-HDM as a function of interior angles α are plotted by solid stars. The solid line shows the analytical dispersions of edge modes for a single corner obtained under quasistatic and small wave number limitations. The blue circles show the numerical results obtained by BEM with quantum corrections under quasistatic limits. (e) The difference between $d_\perp$ and $d_\parallel$ of a single interface for the charge neutral case, p charging ($d_\parallel = -0.001$ nm), and n charging ($d_\parallel = 0.001$ nm) are plotted by red, blue, and green lines, respectively.

is due to the location of the induced charge densities [77,78], which can be discussed using the Feibelman parameter that describes the centroid of the induced charges [67,77,78]. If the induced charges are mainly inside the jellium background, the resonance frequency blueshifts. Conversely, if the induced charge mainly locates outside the jellium background, the resonance frequency redshifts.

We also plot the resonance frequencies of Fa_1^T mode, Fa_1^S mode, and dipole mode as a function of particle size r_a^{-1} in Fig. 7(b) by red, blue, and green lines, respectively. In contrast to the edge modes, the face modes are redshifted with the decreasing of particle size for both the triangle and square. The size dependence of the face modes is found to be similar to that of the dipole mode of cylindrical rods. It can be shown that the quantum corrections to the dipole mode of cylindrical rods are [47,67] (see also Supplemental Material, Sec. IX, for detailed derivations [57])

$$\left(\frac{\omega}{\omega_p}\right)^2 = \frac{1}{2}\left[1 - \frac{1}{r_a}(d_\perp - d_\parallel)\right], \tag{4.1}$$

where $\omega_p^2 = e^2 n_{\text{ion}}/m_e \varepsilon_0$ is the bulk plasma frequency. Here, $d_\perp$ and $d_\parallel$ are the Feibelman parameters defined as

$$d_\perp = \frac{\int x\rho_1 dx}{\int \rho_1 dx}, \quad d_\parallel = \int \frac{n_0 - n_j}{n_{\text{ion}}}dx, \tag{4.2}$$

for a single interface [77,78]. For charge neutral interfaces, $d_\parallel$ is equal to zero, and $d_\perp$ describes the centroid of the charges induced by the external field. The calculated values of $d_\perp - d_\parallel$ are shown in Fig. 7(e) for a sodium neutral flat interface. The interface is at $x = 0$ nm, which is formed by sodium ($x < 0$ nm) and vacuum ($x > 0$ nm). The parameters used in these single interface calculations are the same with all the 2D calculations. It can be seen that, at the dipole resonance frequency (~ 4.0 eV), $d_\perp > 0$, indicating that the resonance frequency of the dipole mode is redshifted [67,77]. Our calculations also numerically verify this point, as shown by the solid green lines in Fig. 7(b). The induced charge densities shown in Fig. 5 of these face modes also mainly reside outside the jellium background, similar to the D mode of cylindrical particles. So the resonance frequencies of the face modes are redshifted within SC-HDM. Furthermore, we also plot the size dependence of the Bennett mode in Fig. 7(c). It shows that the size dependence of the Bennett mode is opposite to the dipole mode, consistent with Ref. [48].

To further investigate the edge modes, we plot the resonance frequencies of the lowest frequency edge modes calculated by SC-HDM as a function α by red stars in Fig. 7(d). For cylindrical particles ($\alpha = 90°$), we plot the resonance frequency of dipole modes. We see that the edge mode frequencies increase monotonically with the interior angles α. To see the

physical reasons, we first recall the analytical dispersions of the even corner modes in the static and small wave number approximations are [65,66] (see also Supplemental Material, Sec. X, for detailed derivations [57])

$$\left(\frac{\omega}{\omega_p}\right)^2 = \frac{\alpha}{\pi}. \qquad (4.3)$$

We plot Eq. (4.3) as a solid line in Fig. 7(d). The qualitative agreement between analytical models and SC-HDM results indicates the resonances in the spectrum are indeed edge modes. The quantitative deviations between these two are due to quantum corrections caused by electron spill-out effect. To quantitatively model this effect, we employ the Feibelman d-parameter model based on the boundary element method (BEM) as defined in Ref. [67] to see the quantum corrections of these edge modes. The numerical results of this quantum BEM are shown by open blue circles in Fig. 7(d). We see excellent agreement between quantum BEM results and SC-HDM results for cylindrical particles. As the wedge angle decreases, both methods show a similar trend of deviation from the classical quasistatics results, indicating the effect of electron spill out. However, the deviation between quantum BEM and SC-HDM results becomes larger for sharper corners. This is because local charging effect causes the $d_\parallel$ to become polar angle dependent, which is inherent in SC-HDM but not included in the quantum BEM model. Nevertheless, quantum BEM still gives the correct shift directions compared with the analytical models. Figure 7(d) reinforces the notion that the edge mode frequencies are very sensitive to the corner angles.

C. Charged particles

The SC-HDM can also be used to treat charged metallic particles. This is a distinct advantage of this method, as there is no obvious way to consider a charged particle within the framework of macroscopic classical electrodynamics. This is also useful as nanosized metallic particles are not necessarily neutral. To study charged particles, we need to carry out the calculations by changing the σ manually in the constraint condition in Eq. (2.7) for ground state calculations. For the sake of computation efficiency, we transform the constraint to the Neumann boundary condition of Eq. (2.5) (see Supplemental Material, Sec. II [57]). During the transformation, we assume that the electrostatic potential ϕ_0 decays isotropically on the boundary $\partial\Omega_G$. This approximation is good when r_g is chosen to be large enough, and we choose the value of r_g to make sure that further increase of r_g does not change the absorption spectrum. The numerical results suggest that it is good to set r_g to be 8.0 nm for 2 nm particles (see Supplemental Material, Sec. XI [57]).

To see the effect of the additional charges on the plasmonic modes, we calculate the absorption cross sections of different charged cylinders, triangles, and squares, as plotted in Figs. 8(a), 8(b), and 8(c), respectively. The incident light is a single plane wave with incident angle $\theta_i = 0$. To make the additional charges σ easier to interpret, we introduce the quantity ΔS defined as $\sigma/en_{\rm ion}$ with the dimension of area in 2D configurations here. Also, $\Delta S > 0$ (<0) stands for positive (negative) charged particles. The ratio of ΔS to the total jellium area means the percentage of additional
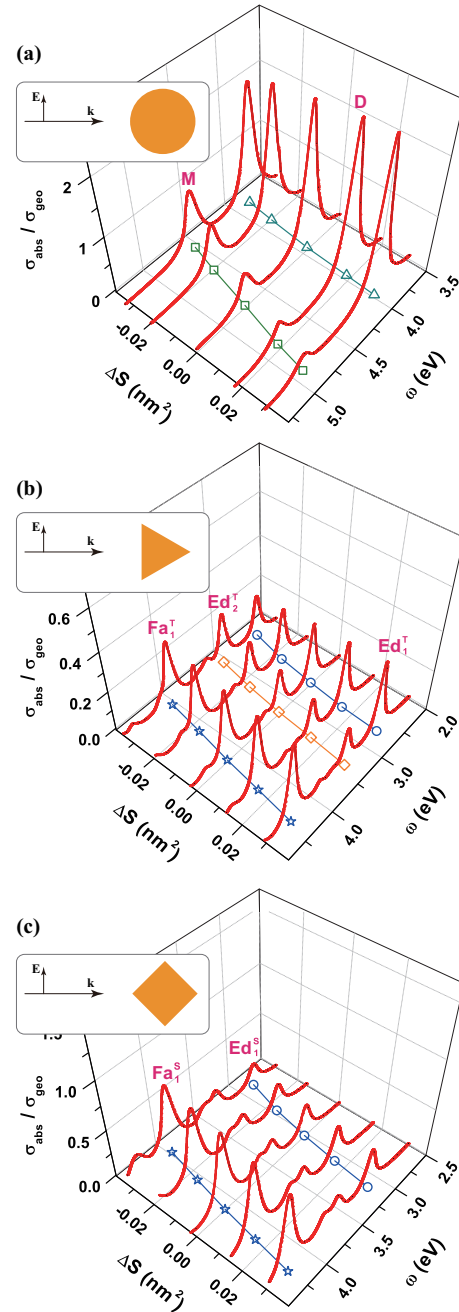

FIG. 8. (a) Absorption spectra of a charged cylinder are shown by solid red lines for different additional amounts of charges. The open cyan triangle dots and open green square dots show the resonance frequencies as a function of ΔS for dipole mode (D) and Bennett mode (M), respectively. The vertical axis is the absorption cross section $\sigma_{\rm abs}$ divided by geometric cross section $\sigma_{\rm geo} = 2r_a$. (b) Absorption spectra of a charged triangle are shown by solid red lines for different additional amounts of charges. The dependence of resonance frequencies on ΔS are shown by open blue circles, open orange square dots, and open blue star dots for the Ed_1^T mode, the Ed_2^T mode, and the Fa_1^T mode, respectively. (c) Absorption spectra of the charged square are shown by solid red lines for different additional amounts of charges. The dependence of resonance frequencies on the amount of ΔS are shown by open blue circles and open blue star dots for the Ed_1^S mode and the Fa_1^S mode, respectively. All the polygons have the same circumradius $r_a = 2.0$ nm, and loss parameter γ is 0.17 eV throughout the domain Ω_D.
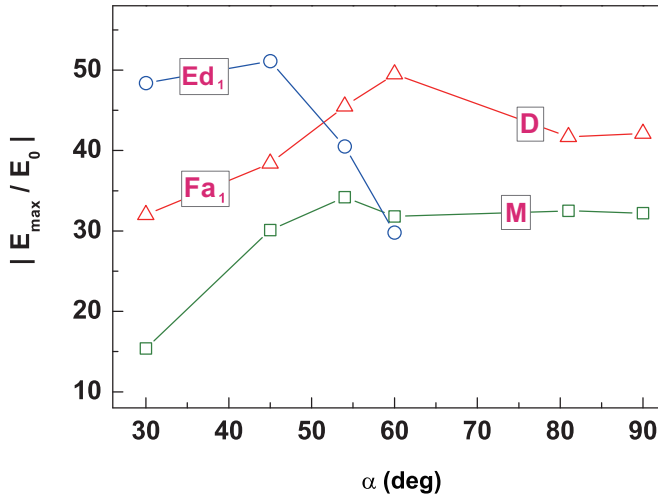
FIG. 9. Electric field enhancement factors of polygonal rods under plane wave illumination ($\theta_i = 0$) as a function of interior angles α for edge modes (blue circles), face modes (red triangles), and Bennett mode (green squares) calculated using SC-HDM. These plasmonic modes correspond to those shown in Fig. 6(a).

number of charge carriers to the total number of charge carriers. Figure 8 shows that all the plasmonic modes are blueshifted in the positive charged particles and redshifted in the negative charged particles. However, the magnitudes of shifting are different for different modes. For the modes with long-range charge oscillations, such as the D mode and face modes, the shifting is small compared to the "local" modes, such as the Bennett mode and edge modes. This is because the additional charges accumulate near the surface and hence create a stronger effect on the surface than the bulk. Furthermore, the changes of the strength of the Bennett mode are most significant in all these plasmonic modes. Since the Bennett mode is locally charge neutral, the doping should have the most prominent effects on this mode.

To illustrate the physics, we calculate and compare the $\mathrm{Re}[d_\perp - d_\parallel]$ of a single interface for charge neutral, positively charged, and negatively charged cases in Fig. 7(e) by red, blue, and green lines, respectively. We see that near the dipole resonance frequency, $\mathrm{Re}[d_\perp - d_\parallel]$ is smaller in the positively charged interface than the neutral interface, so according to Eq. (4.1), the dipole plasmonic mode should blueshift upon positive charging. For the negatively charged interface, $\mathrm{Re}[d_\perp - d_\parallel]$ is bigger than the neutral interface around 4 eV and should induce a red shift. These effects explain the trend for the dipole mode in Fig. 8(a). The Bennett mode corresponds to the zero of $\mathrm{Re}[d_\perp - d_\parallel]$ because of its charge neutral nature. So the resonance frequency of the Bennett mode should blueshift for the positively charged particle, as seen from both Figs. 7(e) and 8(a).

D. Lightning rod effect and energy dissipation distributions

The plasmonic modes of polygonal rods can have useful applications due to their local electric field enhancements. Such a phenomenon is often called the lightning rod effect [79]. We plot the maximum electric fields $\mathbf{E}_{\max}$ normalized by the incident field amplitude $\mathbf{E}_0$ for edge modes, face modes (together with D mode), and the Bennett mode (together with its precursors) by blue circles, red triangles, and green squares in Fig. 9. We see that the field enhancement for face modes and Bennett modes increases with the interior angle α, but the enhancement for edge modes shows an opposite trend. The field enhancements for edge modes and face modes have a crossover between a square rod and a pentagon rod. This is because the polygons with smoother edges carry weaker edge modes and stronger face modes, as shown in Figs. 6(a) and 6(c). We note that the field enhancements shown in Fig. 9 have the same order of magnitude as those obtained using *ab initio* TD-DFT [31,64], indicating that our method gives reasonable results.

The absorption spectra shown earlier are calculated by integrating the fields at the far field. Within the context of the hydrodynamic model, the energy absorption from the
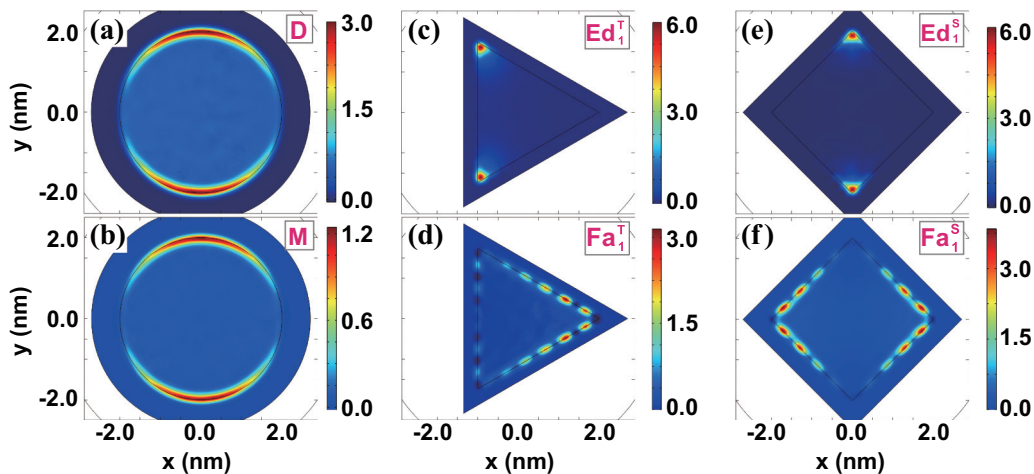

FIG. 10. Contour plot of the energy dissipation $\langle \mathbf{J}_1 \cdot \mathbf{E}_1 \rangle / I_0$ in units of nm^{-1} within the domain Ω_D for (a) dipole mode (D), (b) Bennett mode (M), (c) Ed_1^T mode, (d) Fa_1^T mode, (e) Ed_1^S mode, and (f) Fa_1^S mode. These plasmonic modes correspond to those in Fig. 6(a) with $r_a = 2.0$ nm.

incident light is due to the work done by the EM wave on the electrons. In order to understand the energy dissipation distributions inside the electron gas, we calculate the time averaged work done $W_e = \langle \mathbf{J}_1 \cdot \mathbf{E}_1 \rangle$ by the fields on the electron gas. In our model, this work done could be obtained by the microscopic current $\mathbf{J}_1$ and the microscopic field $\mathbf{E}_1$. As a consistency check, the integration of W_e/I_0 (I_0 is the intensity of incident light) within the domain Ω_D should be equal to the absorption cross section calculated with fields at the far field, and we numerically verify this is indeed the case in Sec. XII in Supplemental Material [57]. To see the distributions work done W_e for different plasmonic modes, we plot in Figs. 10(a)–10(f) the spatial distributions of W_e/I_0 for the plasmonic resonance modes shown in Fig. 6(a), including the dipole mode, the Bennett mode, Ed_1^T mode, Fa_1^T mode, Ed_1^S mode, and Fa_1^S mode. From Fig. 10, we see the dominant loss of all these modes comes from the interface area of the particles, but not from the bulk interior areas. The difference between the modes is similar to the induced electron distributions, namely the energy dissipations mainly come from the edge (face) area for the edge (face) modes. From Figs. 10(d) and 10(f), we find standing-wave-like patterns in the energy dissipation distributions, which further indicate the size dependence of face modes is larger than that of edge modes.

V. CONCLUSIONS

In conclusion, we found three types of plasmonic modes for polygonal metallic particles, including edge modes, face modes, and hybrid modes. These plasmonic modes are classified according to their induced electron concentration profile. We show that the edge modes are less sensitive to particle size than the face modes, but are more sensitive to corner angles of the edges. The edge and face modes can be viewed as broken-symmetry consequences of the dipole mode of a cylindrical particle. As the number of the sides of the polygon increases, the edge mode moves up and the face mode moves down in frequency to merge into the classical dipole plasmonic mode of a cylinder. The hybrid modes are found to be the precursor of the quantum Bennett mode. Finally, it is shown that positive (negative) charging causes the blue (red) shift to all these plasmonic modes.

[1] O. Nicoletti, F. de la Peña, R. K. Leary, D. J. Holland, C. Ducati, and P. A. Midgley, Nature **502**, 80 (2013).

[2] E. Moreno, S. G. Rodrigo, S. I. Bozhevolnyi, L. Martín-Moreno, and F. J. García-Vidal, Phys. Rev. Lett. **100**, 023901 (2008).

[3] J. A. Schuller, E. S. Barnard, W. Cai, Y. C. Jun, J. S. White, and M. L. Brongersma, Nat. Mater. **9**, 193 (2010).

[4] A. Boltasseva and H. A. Atwater, Science **331**, 290 (2011).

[5] J. Chen, M. Badioli, P. Alonso-González, S. Thongrattanasiri, F. Huth, J. Osmond, M. Spasenović, A. Centeno, A. Pesquera, P. Godignon, A. Zurutuza Elorza, N. Camara, F. J. García de Abajo, R. Hillenbrand, and F. H. L. Koppens, Nature **487**, 77 (2012).

[6] Z. Fei, A. S. Rodin, G. O. Andreev, W. Bao, A. S. McLeod, M. Wagner, L. M. Zhang, Z. Zhao, M. Thiemens, G. Dominguez, M. M. Fogler, A. H. Castro Neto, C. N. Lau, F. Keilmann, and D. N. Basov, Nature **487**, 82 (2012).

[7] T. W. Ebbesen, H. J. Lezec, H. F. Ghaemi, T. Thio, and P. A. Wolff, Nature **391**, 667 (1998).

[8] H. J. Lezec, J. A. Dionne, and H. A. Atwater, Science **316**, 430 (2007).

[9] C. Ciracì, R. T. Hill, J. J. Mock, Y. Urzhumov, A. I. Fernández-Domínguez, S. A. Maier, J. B. Pendry, A. Chilkoti, and D. R. Smith, Science **337**, 1072 (2012).

[10] J. A. Scholl, A. L. Koh, and J. A. Dionne, Nature **483**, 421 (2012).

[11] C. S. Levin, C. Hofmann, T. A. Ali, A. T. Kelly, E. Morosan, P. Nordlander, K. H. Whitmire, and N. J. Halas, ACS Nano **3**, 1379 (2009).

[12] L. Lin, M. Zapata, M. Xiong, Z. Liu, S. Wang, H. Xu, A. G. Borisov, H. Gu, P. Nordlander, J. Aizpurua, and J. Ye, Nano Lett. **15**, 6419 (2015).

[13] C. P. Byers, H. Zhang, D. F. Swearer, M. Yorulmaz, B. S. Hoener, D. Huang, A. Hoggard, W.-S. Chang, P. Mulvaney, E. Ringe,

N. J. Halas, P. Nordlander, S. Link, and C. F. Landes, Sci. Adv. **1**, 1500988 (2015).

[14] S. Dodson, M. Haggui, R. Bachelot, J. Plain, S. Li, and Q. Xiong, J. Phys. Chem. Lett. **4**, 496 (2013).

[15] N. Yu, E. Cubukcu, L. Diehl, D. Bour, S. Corzine, J. Zhu, G. Höfler, K. B. Crozier, and F. Capasso, Opt. Express **15**, 13272 (2007).

[16] W. Ding, R. Bachelot, S. Kostcheev, P. Royer, and R. E. de Lamaestre, J. Appl. Phys. **108**, 124314 (2010).

[17] M. Kaniber, K. Schraml, A. Regler, J. Bartl, G. Glashagen, F. Flassig, J. Wierzbowski, and J. J. Finley, Sci. Rep. **6**, 23203 (2016).

[18] T. V. Teperik, P. Nordlander, J. Aizpurua, and A. G. Borisov, Phys. Rev. Lett. **110**, 263901 (2013).

[19] L. Stella, P. Zhang, F. J. García-Vidal, A. Rubio, and P. García-González, J. Phys. Chem. C **117**, 8941 (2013).

[20] T. V. Teperik, P. Nordlander, J. Aizpurua, and A. G. Borisov, Opt. Express **21**, 27306 (2013).

[21] D. C. Marinica, A. K. Kazansky, P. Nordlander, J. Aizpurua, and A. G. Borisov, Nano Lett. **12**, 1333 (2012).

[22] D. K. Gramotnev, A. Pors, M. Willatzen, and S. I. Bozhevolnyi, Phys. Rev. B **85**, 045434 (2012).

[23] S.-W. Chang, C.-Y. Adrian Ni, and S. Lien Chuang, Opt. Express **16**, 10580 (2008).

[24] L. Lin and Y. Zheng, Sci. Rep. **5**, 14788 (2015).

[25] D. Jin, Q. Hu, D. Neuhauser, F. von Cube, Y. Yang, R. Sachan, T. S. Luk, D. C. Bell, and N. X. Fang, Phys. Rev. Lett. **115**, 193901 (2015).

[26] B. N. J. Persson and E. Zaremba, Phys. Rev. B **31**, 1863 (1985).

[27] D. C. Marinica, M. Zapata, P. Nordlander, A. K. Kazansky, P. M. Echenique, J. Aizpurua, and A. G. Borisov, Sci. Adv. **1**, 1501095 (2015).

[28] J. Yan, Z. Yuan, and S. Gao, Phys. Rev. Lett. **98**, 216602 (2007).

[29] B.-J. Wang, Y. Xu, and S.-H. Ke, J. Chem. Phys. **137**, 054101 (2012).

[30] J.-H. Li, M. Hayashi, and G.-Y. Guo, Phys. Rev. B **88**, 155437 (2013).

[31] P. Zhang, J. Feist, A. Rubio, P. Garcia-Gonzalez, and F. J. Garcia-Vidal, Phys. Rev. B **90**, 161407(R) (2014).

[32] W. Yan, M. Wubs, and N. Asger Mortensen, Phys. Rev. Lett. **115**, 137403 (2015).

[33] K. Yabana and G. F. Bertsch, Phys. Rev. B **54**, 4484 (1996).

[34] Y. Luo, A. I. Fernandez-Dominguez, A. Wiener, S. A. Maier, and J. B. Pendry, Phys. Rev. Lett. **111**, 093901 (2013).

[35] Y. Luo, R. Zhao, and J. B. Pendry, Proc. Natl. Acad. Sci. USA **111**, 18422 (2014).

[36] A. I. Fernandez-Dominguez, A. Wiener, F. J. Garcia-Vidal, S. A. Maier, and J. B. Pendry, Phys. Rev. Lett. **108**, 106802 (2012).

[37] G. Toscano, S. Raza, A.-P. Jauho, N. Asger Mortensen, and M. Wubs, Opt. Express **20**, 4176 (2012).

[38] S. Raza, G. Toscano, A.-P. Jauho, M. Wubs, and N. A. Mortensen, Phys. Rev. B **84**, 121412(R) (2011).

[39] G. Toscano, S. Raza, W. Yan, C. Jeppesen, S. Xiao, M. Wubs, A.-P. Jauho, S. I. Bozhevolnyi, and N. Asger Mortensen, Nanophotonics **2**, 161 (2013).

[40] A. Wiener, A. I. Fernandez-Dominguez, A. P. Horsfield, J. B. Pendry, and S. A. Maier, Nano Lett. **12**, 3308 (2012).

[41] W. Zhu, R. Esteban, A. G. Borisov, J. J. Baumberg, P. Nordlander, H. J. Lezec, J. Aizpurua, and K. B. Crozier, Nat. Commun. **7**, 11495 (2016).

[42] R. Esteban, A. Zugarramurdi, P. Zhang, P. Nordlander, F. J. García-Vidal, A. G. Borisov, and J. Aizpurua, Faraday Discuss. **178**, 151 (2015).

[43] R. Esteban, A. G. Borisov, P. Nordlander, and J. Aizpurua, Nat. Commun. **3**, 825 (2012).

[44] S. Zhang, K. Bao, N. J. Halas, H. Xu, and P. Nordlander, Nano Lett. **11**, 1657 (2011).

[45] A. Sobhani, A. Manjavacas, Y. Cao, M. J. McClain, F. Javier García de Abajo, P. Nordlander, and N. J. Halas, Nano Lett. **15**, 6946 (2015).

[46] E. Zaremba and H. C. Tso, Phys. Rev. B **49**, 8147 (1994).

[47] W. Yan, Phys. Rev. B **91**, 115416 (2015).

[48] G. Toscano, J. Straubel, A. Kwiatkowski, C. Rockstuhl, F. Evers, H. Xu, N. Asger Mortensen, and M. Wubs, Nat. Commun. **6**, 7132 (2015).

[49] C. Ciraci and F. Della Sala, Phys. Rev. B **93**, 205405 (2016).

[50] C. Ciraci, Phys. Rev. B **95**, 245434 (2017).

[51] K. Yabana, T. Sugiyama, Y. Shinohara, T. Otobe, and G. F. Bertsch, Phys. Rev. B **85**, 045134 (2012).

[52] S. A. Sato, K. Yabana, Y. Shinohara, T. Otobe, and G. F. Bertsch, Phys. Rev. B **89**, 064304 (2014).

[53] P. Halevi, Phys. Rev. B **51**, 7497 (1995).

[54] *Theory of the Inhomogeneous Electron Gas*, edited by S. Lundqvist and N. H. March (Plenum, New York, 1983).

[55] C. F. v. Weizsäcker, Zeitschrift für Physik **96**, 431 (1935).

[56] E. Wigner, Phys. Rev. **46**, 1002 (1934).

[57] See Supplemental Material at http://link.aps.org/supplemental/10.1103/PhysRevB.96.125134 for details about our model.

[58] P. Gies and R. R. Gerhardts, Phys. Rev. B **31**, 6843 (1985).

[59] C. Voisin, D. Christofilos, N. Del Fatti, F. Vallée, B. Prével, E. Cottancin, J. Lermé, M. Pellarin, and M. Broyer, Phys. Rev. Lett. **85**, 2200 (2000).

[60] X. Li, H. Fang, X. Weng, L. Zhang, X. Dou, A. Yang, and X. Yuan, Opt. Express **23**, 29738 (2015).

[61] Jian-Ming Jin, *The Finite Element Method in Electromagnetics* (John Wiley and Sons, Hoboken, 2014).

[62] COMSOL Multi-physics 4.4, developed by COMSOL Inc. (2013).

[63] C. J. Fall, N. Binggeli, and A. Baldereschi, Phys. Rev. Lett. **88**, 156802 (2002).

[64] J. M. Fitzgerald, S. Azadi, and V. Giannini, Phys. Rev. B **95**, 235414 (2017).

[65] L. Dobrzynski and A. A. Maradudin, Phys. Rev. B **6**, 3810 (1972).

[66] L. Shan, E. G. Mishchenko, and M. E. Raikh, Phys. Rev. B **93**, 085435 (2016).

[67] T. Christensen, W. Yan, A.-P. Jauho, M. Soljačić, and N. A. Mortensen, Phys. Rev. Lett. **118**, 157402 (2017).

[68] A. Mackay, Electron. Lett. **25**(24), 1624 (1989).

[69] S. Viarbitskaya, A. Teulle, R. Marty, J. Sharma, C. Girard, A. Arbouet, and E. Dujardin, Nat. Mater. **12**, 426 (2013).

[70] M. Song, A. Bouhelier, P. Bramant, J. Sharma, E. Dujardin, D. Zhang, and G. Colas-des-Francs, ACS Nano **5**, 5874 (2011).

[71] A. J. Bennett, Phys. Rev. B. **1**, 203 (1970).

[72] K.-D. Tsuei, E. W. Plummer, A. Liebsch, K. Kempa, and P. Bakshi, Phys. Rev. Lett. **64**, 44 (1990).

[73] G. Chiarello, V. Formoso, A. Santaniello, E. Colavita, and L. Papagno, Phys. Rev. B **62**, 12676 (2000).

[74] P. J. Feibelman, Phys. Rev. B **40**, 2752 (1989).

[75] A. Liebsch, Phys. Rev. B **48**, 11317 (1993).

[76] W. L. Schaich, Phys. Rev. B **55**, 9379 (1997).

[77] A. Liebsch, *Electronic Excitations at Metal Surfaces* (Plenum, New York, 1997).

[78] P. J. Feibelman, Prog. Surf. Sci. **12**, 287 (1982).

[79] P. F. Liao and A. Wokaun, The J. Chem. Phys. **76**, 751 (1982).